https://doi.org/10.5194/egusphere-2026-4871
Preprint. Discussion started: 14 August 2026

Seismic Evidence for Increasing Unfrozen Pore Water Heterogeneity from Roadside to Coastal Arctic Tundra

Guilherme Zakarewicz[1], Gabriel Rocha dos Santos[1], Eileen R. Martin[2], Ming Xiao[3], and Tieyuan Zhu[1]

[1]Department of Geosciences, The Pennsylvania State University, University Park, PA, USA
[2]Department of Geophysics, Department of Applied Math and Statistics, Colorado School of Mines, Golden, CO, USA
[3]Department of Civil and Environmental Engineering, The Pennsylvania State University, State College, PA, USA

Correspondence: Tieyuan Zhu (tyzhu@psu.edu)

Abstract. Permafrost contains liquid pore water even at subzero temperatures, and the partitioning between pore ice and unfrozen water governs its mechanical and hydrological properties. Resolving this partitioning at depth and across short lateral distances remains challenging because direct subsurface observations are spatially sparse. Here, we apply active-source multichannel analysis of surface waves (MASW) using a long-term distributed acoustic sensing (DAS) cable and conventional geophone arrays at five sites along a ∼2 km transect in Utqiaġvik, Alaska, that captures a transition from a disturbed roadside environment to the Arctic coast. Shear-wave velocity profiles are converted to seismically inferred unfrozen pore water content (S_w) using a load-bearing effective-medium framework and compared against a depth-dependent reference constructed from local borehole temperatures and laboratory freezing curves measured on permafrost cores. Departures from this reference are spatially organized. The DAS-derived departure metric increases toward the coastal end of the transect, while the geophone-derived profiles show greater variability but also identify the site closest to the coast (Tundra 4) as having the largest departure. At this site, the DAS-derived profile remains higher than the temperature reference through much of the deeper section. These results suggest that temperature and shallow laboratory measurements alone do not fully explain the observed permafrost structure, particularly beneath water-rich coastal tundra surfaces characterized by ponds and lakes. The framework introduced here provides a transferable approach for integrating seismic, thermal, and laboratory data to characterize spatially variable permafrost at depth in locations where the reference estimate process would be expected to deviate most from true subsurface conditions.

1 Introduction

Arctic permafrost underlies roughly 20% of the Northern Hemisphere land surface (Obu et al., 2019; Brown et al., 1997) and plays a central role in soil hydrology, surface morphology, and global carbon storage (Hugelius et al., 2014; Schaefer et al., 2014). Arctic warming, which is occurring nearly four times faster than the global average (Rantanen et al., 2022; AMAP, 2021), is accelerating permafrost degradation, with documented consequences including subsidence, infrastructure damage, and release of organic carbon as CO_2 and CH_4 (Nelson et al., 2001; Schuur et al., 2008; Grosse et al., 2011). Although permafrost is defined by temperature, its physical properties depend critically on the partitioning between pore ice and unfrozen liquid water, a quantity that temperature alone does not determine. Sediment texture, mineralogy, pore-size distribution, salinity,

https://doi.org/10.5194/egusphere-2026-4871
Preprint. Discussion started: 14 August 2026

and depositional and hydrological history all influence how much liquid water persists at subzero temperatures (Romanovsky and Osterkamp, 2000; Xiao et al., 2020; Dou et al., 2017), producing ice–water distributions that can vary substantially over short lateral distances even under similar thermal regimes.

Resolving this partitioning at depth and across short lateral distances remains an open problem. In situ observations, such as temperature boreholes and active-layer probing, are spatially sparse and restricted to the near surface (Romanovsky et al., 2010; Biskaborn et al., 2019). Remote sensing identifies landscape expressions of permafrost change such as thermokarst and subsidence, but does not directly constrain the subsurface physical state (Bartsch et al., 2023; Zwieback et al., 2024). Deep thaw features such as taliks can develop beneath lakes, disturbed surfaces, and zones of lateral heat or solute transport, reaching depths of tens of meters (Pedrazas et al., 2020; Angelopoulos et al., 2021; Ke et al., 2025), yet their spatial organization is difficult to resolve from surface observations alone. Coastal permafrost is a particularly relevant setting: marine deposition, saline groundwater, and hydrological exchange with the ocean provide additional controls on ice–water partitioning that are absent at sites farther from the shoreline. Hence, such controls raise the question of whether, and how, subsurface heterogeneity is organized along a roadside-to-coast transect.

Geophysical methods, including seismic surface-wave analysis and electrical resistivity tomography, offer a path toward characterizing subsurface properties over larger spatial volumes (Keating et al., 2018; Oldenborger and LeBlanc, 2018; Liu et al., 2022). However, seismic velocities and electrical resistivities in partially frozen sediments respond simultaneously to unfrozen pore water content, porosity, salinity, sediment texture, and cryostructure (Ji et al., 2024; Dou et al., 2017), making spatial variability in these properties ambiguous when considered in isolation. Temperature-based estimates of ice–water partitioning in freezing soils conventionally rely on a soil freezing characteristic curve (SFCC), which relates unfrozen water content to temperature and forms the basis of physically based freeze–thaw models (Devoie et al., 2022). Therefore, a departure from a temperature-informed expectation provides a sharper diagnostic: if the seismically inferred unfrozen water content exceeds what local temperature and laboratory freezing curves would predict, additional controls must be involved. Here, we combine a local borehole temperature profile with laboratory-derived freezing curves from permafrost cores distributed along a ∼2 km transect (Wang et al., 2025) to construct a depth-dependent, temperature- and laboratory-informed reference profile of unfrozen pore water content, $S_{w,\mathrm{ref}}(z)$. This reference represents a one-dimensional thermal and laboratory-based regional expectation against which the seismic profiles are evaluated, allowing us to separate anomalous ice–water partitioning from the background thermal signal.

We present active-source multichannel analysis of surface waves (MASW) surveys acquired along a ∼2 km transect in Utqiaġvik, Alaska, using both a long-term distributed acoustic sensing (DAS) fiber-optic cable and conventional geophone arrays at five discrete sites that capture a transition from a disturbed roadside environment to the Arctic coast. Shear-wave velocity (V_s) profiles derived independently from both sensing systems are converted to unfrozen pore water content using a load-bearing effective-medium rock-physics framework (Helgerud et al., 1999; Mavko et al., 1998; Dvorkin and Nur, 1996) and compared against reference $S_{w,\mathrm{ref}}(z)$ estimated from thermal data. The resulting anomalies between reference and seismically inferred profiles are spatially organized, with modest departures at the roadside and inland tundra sites (Roadside–Tundra 2), a shallower anomaly at the intermediate site (Tundra 3), and the strongest DAS-derived anomaly at the site closest to the coast

https://doi.org/10.5194/egusphere-2026-4871
Preprint. Discussion started: 14 August 2026

(Tundra 4). This pattern indicates that water-rich coastal tundra surfaces, characterized by ponds and lakes, are associated with stronger and more depth-persistent unfrozen pore water anomalies than the drier roadside and inland tundra sites.

2 Data and Methods

2.1 Study Location

The study was conducted in Utqiaġvik, Alaska, along a 2 km distributed acoustic sensing (DAS) cable deployed in September 2021. The cable has continuously recorded ambient seismic signals since deployment, providing dense spatial sampling for near-surface monitoring, and has enabled cryospheric and solid-Earth observations in the area (Rocha dos Santos and Zhu, 2025).

The cable follows a short segment along a gravel road and then continues into the adjacent undisturbed tundra toward the coast (Figure 1). This setting covers contrasting surface environments, ranging from a disturbed roadside to undisturbed coastal tundra over a short lateral distance. Thus, it provides several independent opportunities to test whether subsurface unfrozen water content tracks the local thermal regime or indicates additional controls. Previous studies indicate that permafrost in the region is approximately 200–400 m thick (Jorgenson et al., 2008), while the active layer typically varies from about 0.1 to 0.6 m depending on local surface and hydrologic conditions (Jafarov et al., 2018; Tourei et al., 2024; Wang et al., 2025). The landscape along this section is characterized by polygonal ground with ice-wedge networks, low-relief microtopography, ponded or wet areas, and thermokarst lakes. These features are relevant to our analysis because water-rich environments can enhance heat transfer into the subsurface and promote lateral hydrologic exchange (Freitas et al., 2025; in 't Zandt et al., 2020; Jones et al., 2023). In this study, we focus on five discrete locations along the transect (sections Roadside and Tundra 1–4) chosen to capture this transition from roadside to undisturbed coastal tundra.

2.2 MASW-derived V_s profiles from DAS and geophones

We analyzed two independent active-source MASW datasets acquired within the same five sites: a DAS survey collected in August 2024 and a conventional geophone survey acquired in August 2022. In both campaigns, seismic energy was generated using sledgehammer impacts, and the resulting data were used to estimate 1D shear-wave velocity (V_s) profiles from surface-wave dispersion (Park et al., 1998, 1999). Although the DAS and geophone acquisitions targeted the same site areas, they were not exactly co-located; instead, the paired observations at each site are separated by short lateral offsets of approximately 5-45 m (Table S4).

Because the datasets were acquired in different years and with different sensor geometries, we do not interpret the paired profiles as exact repeat measurements or as a direct time-lapse signal. Instead, we treat the DAS and geophone profiles as independent observations of the same general subsurface volume, and use their agreement or disagreement at each site as a conservative check on the robustness of the spatial patterns we report below.

https://doi.org/10.5194/egusphere-2026-4871
Preprint. Discussion started: 14 August 2026

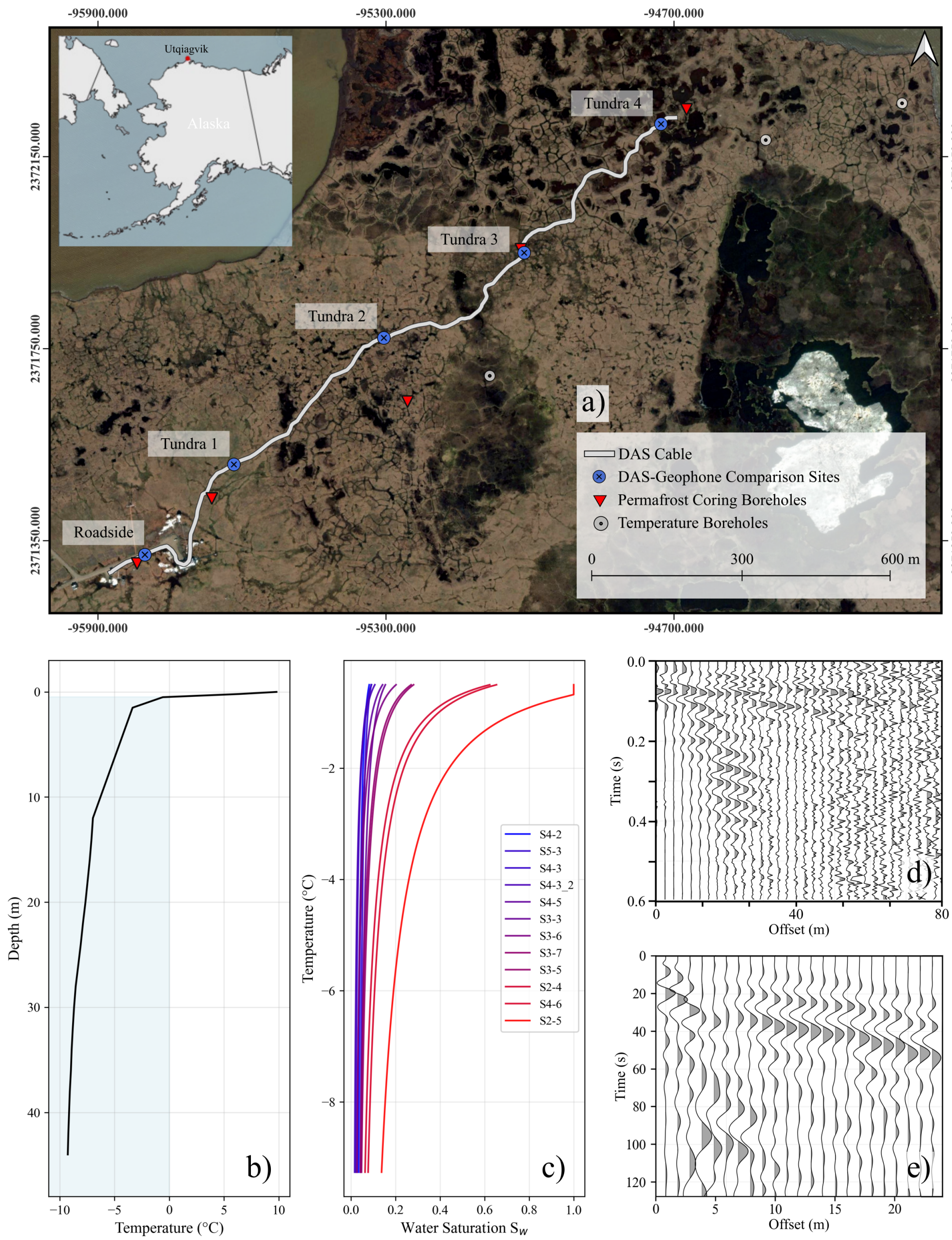

Figure 1. (a) Study area in Utqiaġvik, Alaska. The white line shows the 2 km buried DAS cable deployed in 2021, and crosses mark the five active-source MASW sites (Roadside and Tundras 1–4) used in this study. Gray circles mark temperature boreholes, and red triangles indicate permafrost coring boreholes used for the unfrozen pore water content reference. (b) Temperature profile used to characterize the local thermal regime. (c) Unfrozen pore water content values estimated from laboratory measurements on permafrost core samples reported by Wang et al. (2025). (d) Example DAS shot gather and (e) example geophone shot gather used for surface-wave analysis. The base map was designed and developed by Esri | Powered by Esri. For more information on this map, visit https://goto.arcgisonline.com/maps/World_Imagery (last access: 13 August 2026).

https://doi.org/10.5194/egusphere-2026-4871
Preprint. Discussion started: 14 August 2026

For both datasets, records were preprocessed and transformed into frequency–phase velocity dispersion images using the phase-shift method. Fundamental-mode dispersion curves were manually picked and inverted using the Dinver package in Geopsy (Wathelet et al., 2020). For each site and acquisition type, we retained the 1000 best-fitting models; their median defines the representative V_s profile, and their distribution defines the uncertainty bounds shown in Figures 2 and 5. Additional acquisition parameters, survey geometry, and processing details are provided in the Supplementary Information (Sections S1 and S2). The maximum model depth (40 m) reflects the layer-thickness parameterization used in the Neighborhood Algorithm search and does not by itself indicate that the dispersion data resolve structure to that depth. For each site and sensor, we therefore additionally estimated the depth range independently constrained by the observed dispersion curve using Rayleigh-wave phase-velocity sensitivity kernels (Figure S8, Table S8), which we use in Sect. 4.2 to qualify the interpretation of results within the fixed 0-40 m model space.

2.3 Rock-physics framework and physical constraint

To translate the V_s profiles into a physically interpretable measure of unfrozen pore water content (hereafter S_w), we used the load-bearing effective-medium model (Helgerud et al., 1999; Mavko et al., 1998; Dvorkin and Nur, 1996) relating V_s to the partitioning of pore ice and unfrozen pore water. We evaluated this choice against four alternative V_s-S_w formulations (Zimmerman and King, 1986; Minshull et al., 1994; Dou et al., 2017; Carcione and Seriani, 1998), applied to the seismic profiles using a constant porosity of 0.4 for consistency across models (Figure S3).

In the load-bearing framework, pore ice is treated as part of the load-bearing solid frame rather than as a pore fluid. For an initial (thaw-state) porosity ϕ_0 and ice saturation S_i, the pore volume still available to liquid water is therefore

$$\phi(S_i) = \phi_0(1 - S_i) = \phi_0 S_w, \tag{1}$$

so increasing pore ice content increases the effective stiffness of the medium, whereas increasing S_w reduces the ice-bonded frame contribution and tends to lower V_s. Since the mapping from V_s to S_w is non-unique, we regularized the inversion using a temperature-derived reference profile based on laboratory measurements from nearby cores derived from Wang et al. (2025) (Figure 1c). These measurements were combined with the local borehole temperature profile to construct a depth-dependent reference representing the S_w expected under the local thermal regime. This reference profile was used as a physical constraint rather than site-specific ground-truth. Full details of the load-bearing model and rock-physics framework are provided in the Supplementary Information (Section S3).

Because the V_s-S_w relationship is sensitive to porosity, we first performed a site-specific joint inversion in which each DAS–geophone pair shared a single depth-dependent porosity profile. For each site, we solved for the $\phi_0(z)$ that minimizes

$$\begin{aligned} J(\phi_0) = &\sum_z w_{\text{geo}} \left[S_w^{\text{geo}}(z, \phi_0(z)) - S_w^{\text{ref}}(z)\right]^2 + \sum_z w_{\text{DAS}} \left[S_w^{\text{DAS}}(z, \phi_0(z)) - S_w^{\text{ref}}(z)\right]^2 \\ &+ \lambda \sum_z \left(\frac{d\phi_0}{dz}\right)^2 + \mu \sum_z \left[\phi_0(z) - \phi_{\text{prior}}(z)\right]^2, \end{aligned} \tag{2}$$

https://doi.org/10.5194/egusphere-2026-4871
Preprint. Discussion started: 14 August 2026

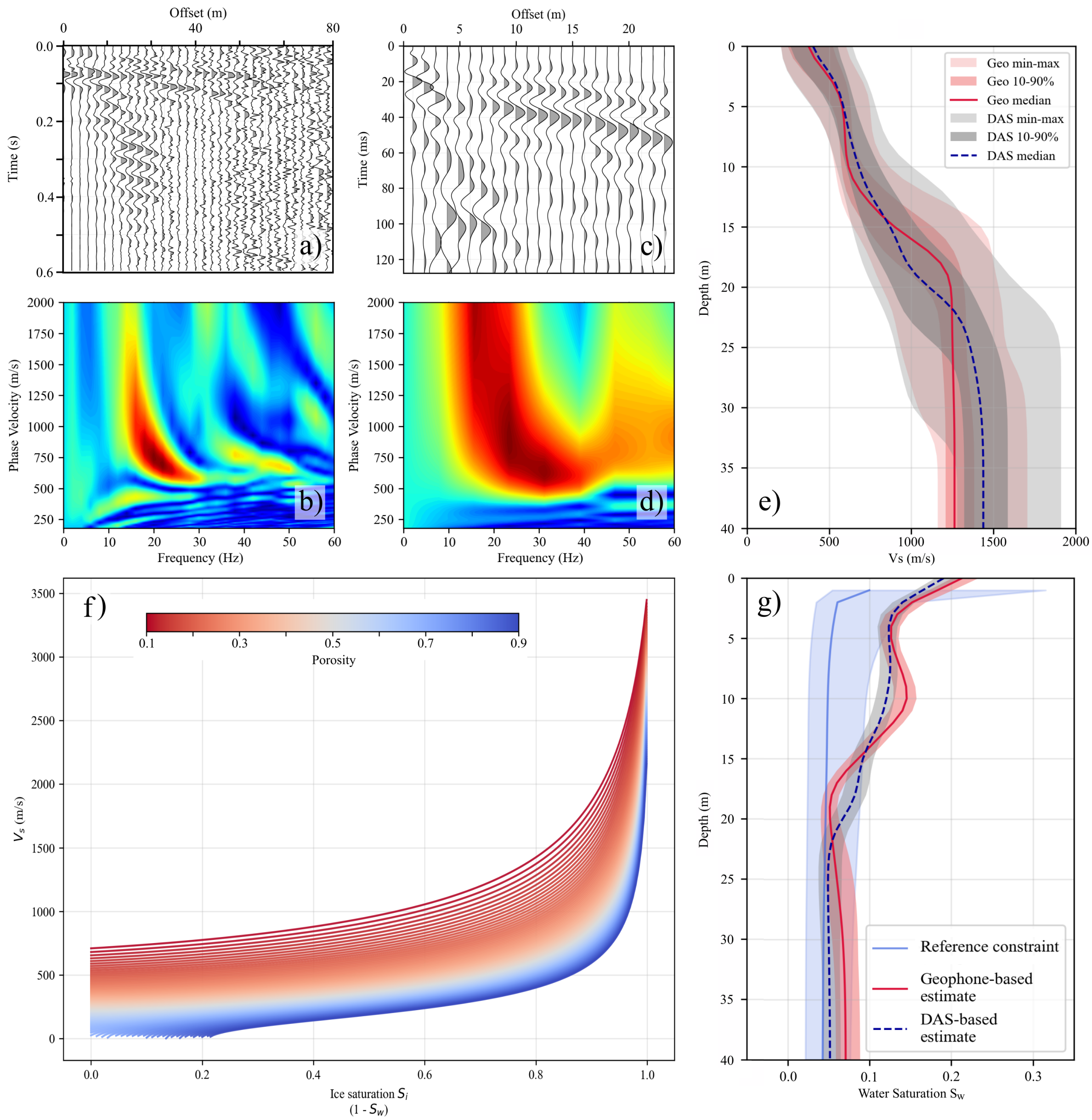

Figure 2. Workflow used to derive V_s profiles and unfrozen pore water content estimates from DAS and geophone data. (a) Seismic data from a DAS shot gather; (b) Corresponding DAS dispersion image generated after the phase shift method; (c) Seismic data from a geophone shot gather; (d) Corresponding geophone dispersion image; (e) MASW-derived V_s profiles, with uncertainty bounds derived from the ensemble of best-fitting models; (f) Load-bearing rock-physics relationship between ice saturation and V_s for varying porosity. (g) Unfrozen pore water content S_w estimates derived from the V_s profiles together with the laboratory and temperature reference constraint. The reference is derived by applying the fitted freezing curves from shallow core samples to the borehole temperature profile. It is therefore a temperature-based extrapolated reference, not a direct deep measurement.

https://doi.org/10.5194/egusphere-2026-4871
Preprint. Discussion started: 14 August 2026

where $S_w^{\text{geo}}(z,\phi_0)$ and $S_w^{\text{DAS}}(z,\phi_0)$ are the unfrozen pore water content profiles predicted from the geophone- and DAS-derived V_s profiles for a given porosity. The first two terms of Eq. (2) pull both the DAS- and geophone-derived S_w profiles toward the common reference $S_w^{\text{ref}}(z)$; the third term imposes vertical smoothness on the porosity profile; and the fourth term penalizes deviations from a prescribed porosity prior $\phi_{\text{prior}}(z)$ (Supplementary Information, Section S4). By requiring each DAS–geophone pair to share the same porosity profile, this step prevents the two V_s profiles at a given site from being mapped to different S_w profiles solely by assigning them independent porosity structures. Because $S_w^{\text{ref}}(z)$ enters directly into the first two terms of Eq. (2), the optimization favors porosity profiles that make both S_w^{geo} and S_w^{DAS} as consistent as possible with the reference at each depth. Hence, the resulting porosity is the one that comes closest to reconciling the observed V_s with $S_w^{\text{ref}}(z)$. The reference-relative anomalies reported below (Sect. 3.4) are therefore the residual departures that remain even after this pull toward the reference, rather than an independent measurement of S_w.

The five optimized porosity profiles were then averaged to define a common porosity reference for the transect, which was used in the final forward mapping from V_s to S_w. This approach reduces the extent to which paired differences can be explained by independently varying porosity profiles.

3 Results

3.1 Local thermal and laboratory observations define an unfrozen pore water reference

Following the approach described in Section 2.3, we combined the local borehole temperature profile with laboratory freezing curves from permafrost cores collected near the DAS transect to construct a depth-dependent, temperature-informed reference for S_w (Fig. 3c). For each core sample, the volumetric unfrozen water content θ_u was normalized by the total volumetric water content θ_w,

$$\theta_{n,u} = \frac{\theta_u}{\theta_w}, \tag{3}$$

such that $\theta_{n,u}$ represents the fraction of the total sample pore water that remains unfrozen at a given temperature. Under the adopted assumption that the pore space is occupied by ice and liquid water, we treat $\theta_{n,u}$ as an observational analogue of the model variable S_w. The laboratory measurements show variability among the measured freezing curves, especially near the freezing point, but progressively lower and more closely grouped unfrozen water content at colder temperatures (Fig. 3a,b).

The fitted freezing curves for the individual samples give unfrozen pore water content as a function of temperature alone, $\theta_{n,u}^{(j)}(T)$ (Fig. 3b), so converting each curve into a function of depth requires only the local temperature at that depth. We therefore evaluated every fitted curve at the temperature predicted by the local borehole profile, $T(z)$ (Fig. 3c), substituting $T(z)$ for T in each sample's fitted relationship to obtain a depth-dependent $\theta_{n,u}^{(j)}(z)$ for every core sample (Fig. 3d, thin colored lines). At each depth, we then took the median of these depth-converted curves across all samples to define the laboratory- and temperature-informed reference profile (blue line),

https://doi.org/10.5194/egusphere-2026-4871
Preprint. Discussion started: 14 August 2026

$$S_{w,\mathrm{ref}}(z) = \mathrm{median}_j \left[\theta^{(j)}_{n,u}(T(z)) \right], \quad (4)$$

treating $\theta_{n,u}$ as an observational analogue of S_w.

The reference is first defined at 0.5 m depth, where the median unfrozen pore water content is 0.163 and the p10–p90 range is 0.086–0.580. The median decreases rapidly to 0.058 at 5 m depth and then changes more gradually, reaching 0.046 at 20 m and 0.043 at 40 m. The corresponding p10–p90 range narrows to 0.024–0.087 at 20 m and 0.022–0.076 at 40 m.

Therefore, the resulting profile predicts nonzero S_w values below the active layer, with most of the depth-dependent decrease occurring within the upper several meters. Below approximately 10 m, the reference approaches comparatively low depth-varying values. This profile is not a direct measurement of deep S_w at depths below the shallow core interval; rather, it is the expected trend with depth if temperature and shallow laboratory freezing behavior were the dominant controls on ice–water partitioning. In the sections that follow, we use this profile as the null hypothesis against which the seismic-derived S_w structures are evaluated.

Because SFCCs underlie most physically based estimates of ice–water partitioning in freezing soils, we compared our fitted local freezing curves with the Devoie et al. (2022) repository of measured SFCCs, which includes 416 curves from 254 publications. This comparison was used as an independent plausibility check, rather than as an additional calibration constraint. Our local curves and the resulting reference profile fall within the broad range spanned by published SFCC measurements (Fig. 4), supporting their use as a physically reasonable temperature-based constraint for this site.

3.2 Seismic profiles show depth-dependent structure across the transect

Surface-wave inversions from the DAS and geophone surveys reveal a clear increase in depth-dependent structural complexity from the roadside toward the coast (Fig. 5). Both datasets were processed within a common workflow and modeled over a common 0-40 m modeled depth range. The sensitivity kernels and estimated depth ranges are shown in Figure S8 and Table S8. Because the inversion parameterizes velocity structure over this fixed 0–40 m interval regardless of what the dispersion data can actually constrain, we separately quantified, for each site and sensor, the depth range over which the observed dispersion curve retains meaningful sensitivity to V_s. We computed the sensitivity of the fundamental-mode Rayleigh-wave phase velocity to V_s, $\partial c/\partial V_s(z)$, for the median DAS and geophone V_s profile at each site, and defined the resolution depth as the depth at which the frequency-integrated sensitivity decays to 10% of its peak value (Figure S8). Resolution depths vary by site and by sensor (Table S8): DAS profiles are resolved to depths ranging from approximately 21 m (Tundra 3) to beyond the full 40 m model space (Tundra 2 and Tundra 4), while geophone profiles are resolved to depths ranging from approximately 20 m (Roadside) to 33 m (Tundra 1). Based on this range, we adopted a common, conservative 0–20 m window to compare the paired DAS–geophone V_s and S_w profiles (Tab. 1).

All five locations exhibit relatively low V_s near the ground surface and an overall increase in velocity with depth, although the magnitude, gradient, and depth of the velocity transitions vary along the transect. At Roadside, Tundra 1, and Tundra 2, the profiles generally show gradual increases through the upper 25 m. The DAS- and geophone-derived median profiles

https://doi.org/10.5194/egusphere-2026-4871
Preprint. Discussion started: 14 August 2026

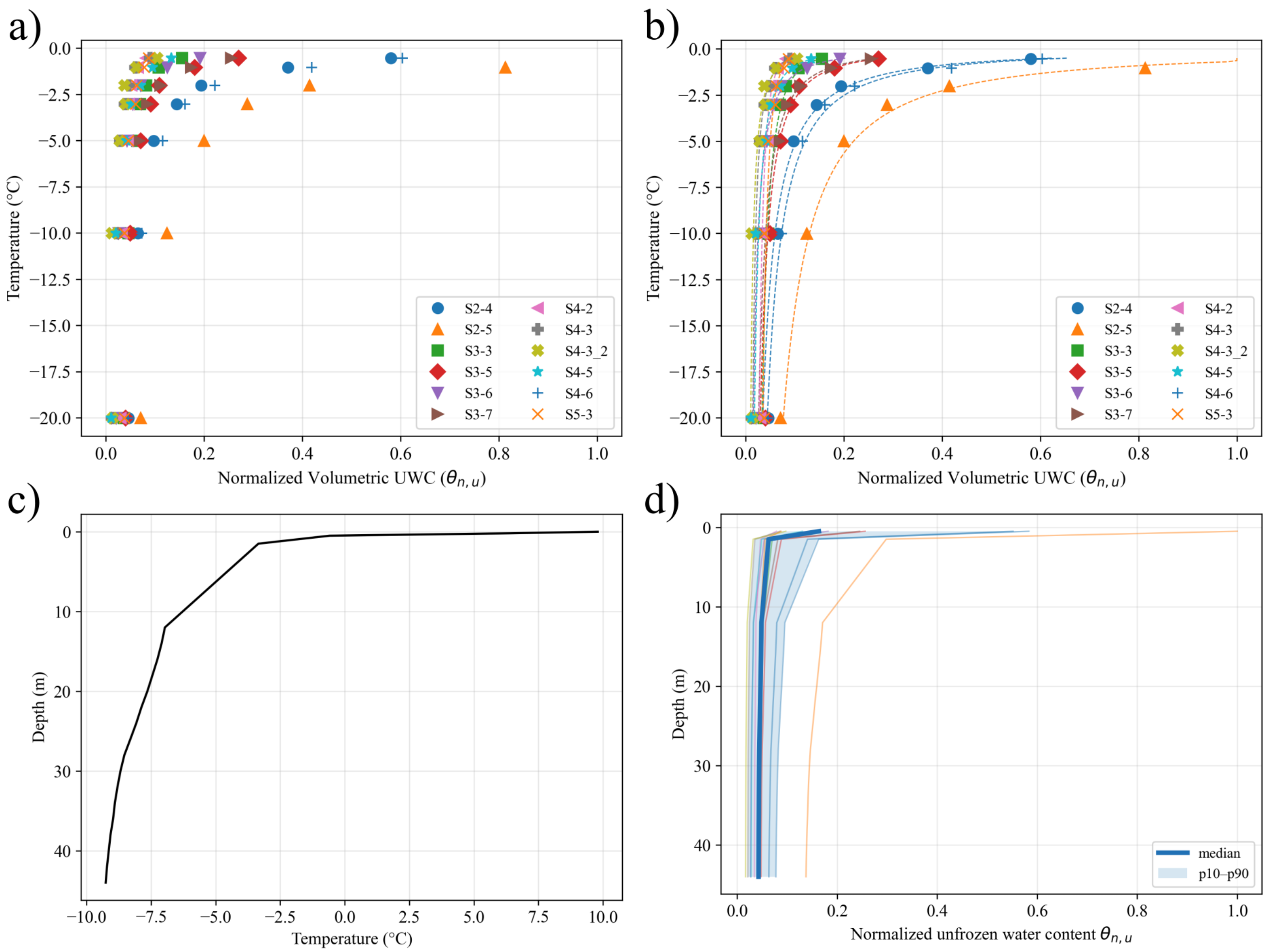

Figure 3. Construction of the unfrozen pore water content reference profile used in the V_s–S_w mapping. (a) Normalized volumetric unfrozen water content $\theta_{n,u}$ measured by Wang et al. (2025) as a function of temperature for permafrost core samples collected near Utqiaġvik. (b) Power-law curves fitted to the laboratory measurements for each sample. (c) Local borehole temperature profile used to convert the temperature-dependent laboratory relationships into depth-dependent profiles. (d) Depth-dependent $\theta_{n,u}$ profiles obtained by evaluating each fitted curve using the local borehole temperature profile. The median curve and p10–p90 range define the reference profile and envelope used in this study. Thin colored curves show the fitted freezing curve for each core sample evaluated along the temperature profile.

https://doi.org/10.5194/egusphere-2026-4871
Preprint. Discussion started: 14 August 2026

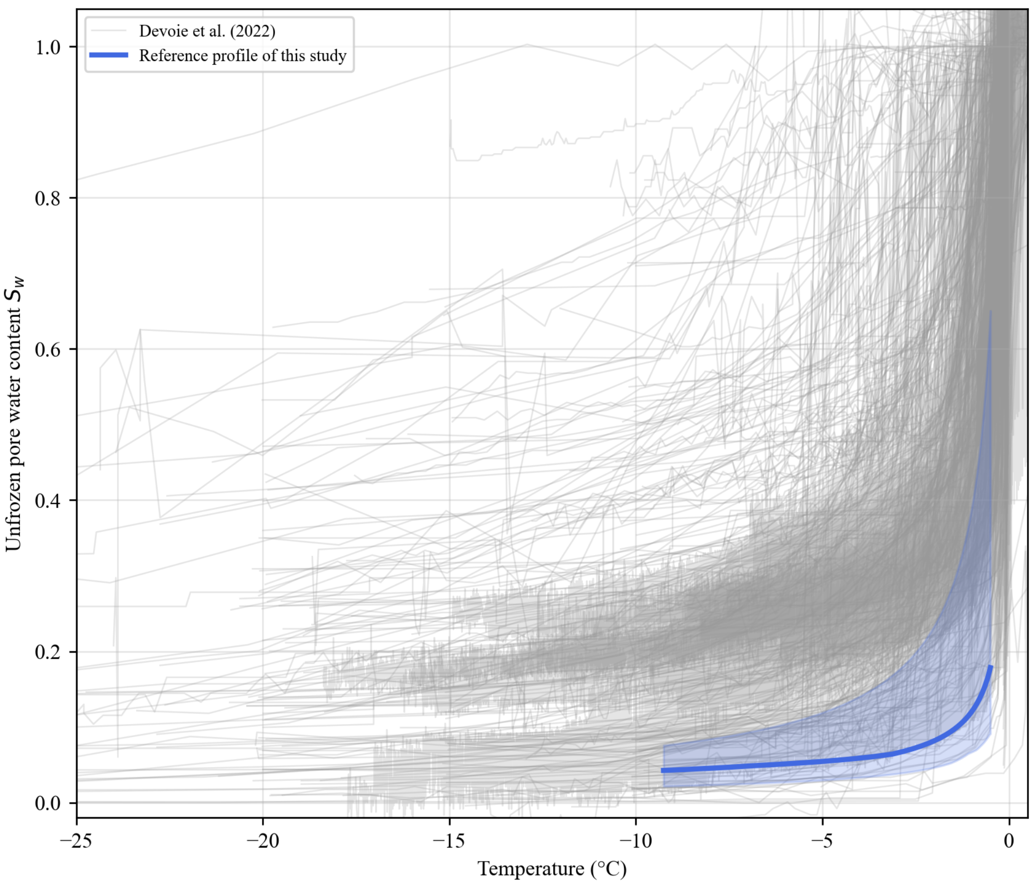

Figure 4. Comparison of the reference profile against the Devoie et al. (2022) repository of measured soil freezing characteristic curves (SFCCs; n = 416, digitized from 254 publications between 1921–2021). The reference profile falls within the range spanned by this independently compiled literature dataset, supporting its use as a physically plausible constraint on unfrozen pore water content.

recover similar first-order vertical trends at these sites, particularly in the shallow subsurface, although differences become more apparent over selected depth intervals. At greater depths, the profiles commonly approach velocities of approximately 1200–1500 m/s.

More abrupt vertical velocity transitions occur at Tundra 3 and Tundra 4. At Tundra 3, both profiles indicate a pronounced increase in V_s between approximately 15 and 25 m, but the transition occurs at different depths and with different gradients in the DAS and geophone results. At Tundra 4, the geophone-derived V_s profile increases sharply between approximately 12 and 18 m and remains near 1200 m/s below this transition. In contrast, the DAS-derived V_s profile remains below approximately 600 m/s through much of the upper 20 m, with a sharp increase after 25 m approaching 1000 m/s. Here, Tundra 4 shows the largest separation between the paired profiles over the investigated depth interval. The root-mean-square differences between

https://doi.org/10.5194/egusphere-2026-4871
Preprint. Discussion started: 14 August 2026

the paired V_s profiles show that the magnitude of the short-offset contrast is not uniform along the transect. The RMSD values, computed over a conservative 0-20 m window (Tab. 1), are 84.7, 125.4, and 107.2 m/s for Roadside, Tundra 1, and Tundra 2, showing comparable differences. However, the values increase to 264.5 m/s at Tundra 3 and 283.8 m/s at Tundra 4, with substantially larger contrasts.

The DAS and geophone profiles are separated laterally by approximately 5-45 m (Table S4) and were obtained using different acquisition geometries and sensing systems. Previous controlled MASW comparisons have shown that well-coupled buried DAS arrays can recover surface-wave dispersion data and V_s profiles closely consistent with conventional geophone or nodal-array measurements (Vantassel et al., 2022; Ma et al., 2026). We therefore interpret the large site-dependent differences observed here as unlikely to arise solely from sensor type, while acknowledging differences in acquisition geometry and survey year. The paired profiles are accordingly interpreted as observations of adjacent local subsurface volumes rather than as exact repeat measurements of the same one-dimensional structure. This allows us to assess the short-offset variability at each site.

3.3 Seismically inferred unfrozen pore water profiles show site-dependent paired contrasts

To evaluate how the observed velocity differences translate into the modeled ice–water partitioning, we converted the paired nearby location V_s profiles into unfrozen pore water content, S_w, using the adopted load-bearing rock-physics framework (Sections S3–S5 of Supplementary Information). The resulting profiles are shown in the lower panels of Fig. 5. Under the saturated ice–water pore model, larger S_w values indicate that a greater proportion of the pore volume is occupied by unfrozen water (liquid phase). These profiles are model-derived quantities rather than direct measurements of unfrozen pore water content and depend on the assumptions and parameters of the rock-physics mapping.

The inferred S_w profiles preserve the main spatial pattern observed in the V_s comparisons. Roadside, Tundra 1, and Tundra 2 show comparatively small paired differences, whereas Tundra 3 and especially Tundra 4 show larger contrasts. The strongest paired contrast occurs at Tundra 4, where the profile from the array offset by $\sim$36 m from the geophone deployment (DAS; Figure S1) indicates substantially higher modeled unfrozen pore water content over much of the intermediate-depth interval. Detailed paired-profile metrics are reported in Tab. 1. Because the paired profiles were acquired with different sensors, geometries, and acquisition years, these differences are not interpreted as direct time-lapse changes. Instead, their site dependence is most consistent with stronger small-scale subsurface heterogeneity at the coastal end of the transect.

3.4 Differences between seismic-inferred and reference unfrozen pore water profiles with depth

Interfacial effects, pore-size distribution, mineral surface chemistry, and dissolved solutes allow liquid water to persist under subzero conditions (Romanovsky and Osterkamp, 2000), and the reference profile reflects this by predicting nonzero S_w throughout the investigated depth. Because the absolute S_w values depend on the rock-physics model, we focus on the difference between the seismic-inferred profile and the common temperature and laboratory reference.

To determine whether the seismic-inferred unfrozen pore water content remains consistent with the local temperature-informed reference, we calculated the depth-dependent difference between the median seismic-derived and reference profiles:

https://doi.org/10.5194/egusphere-2026-4871
Preprint. Discussion started: 14 August 2026

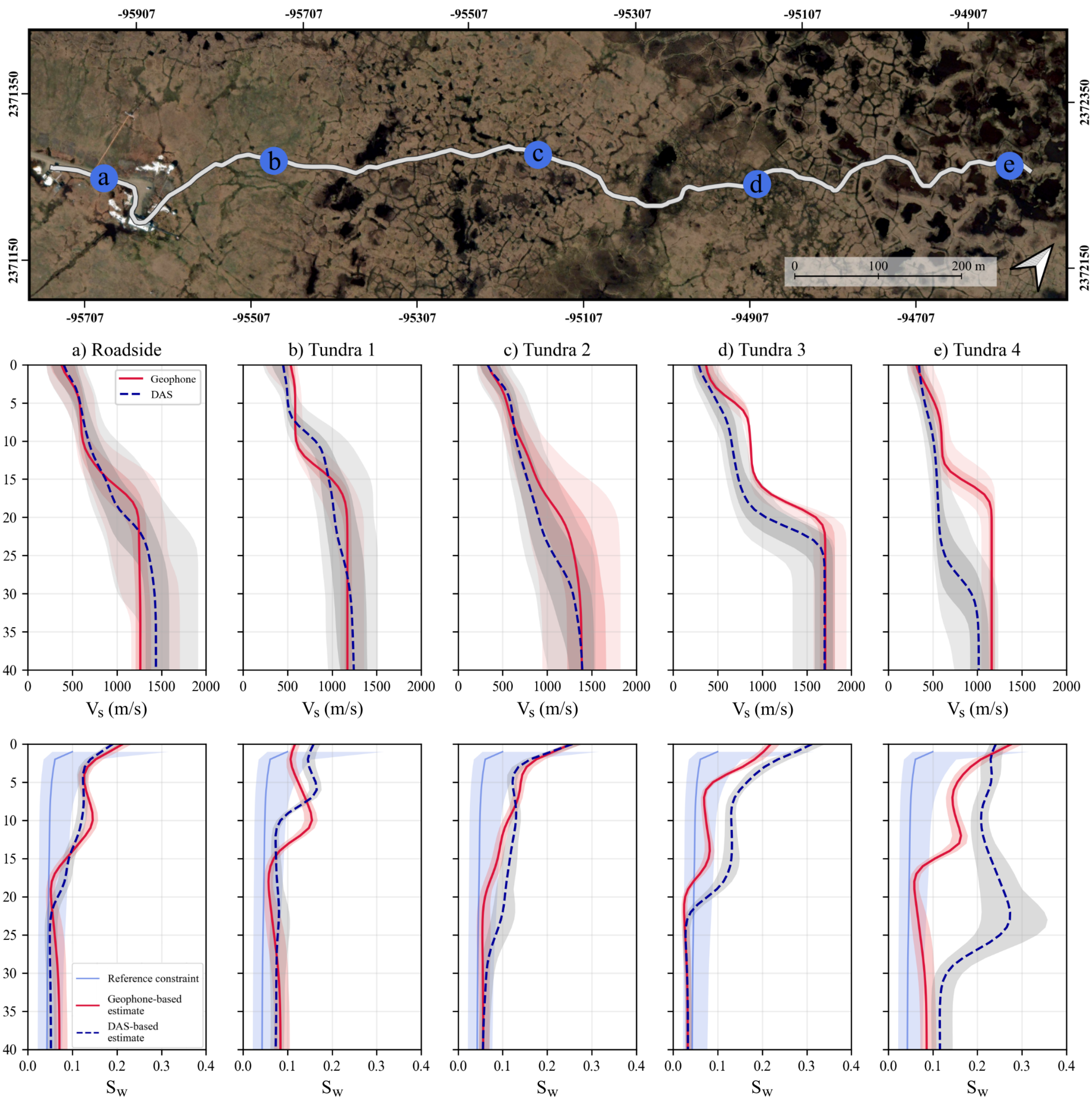

Figure 5. Comparison of V_s and estimated S_w profiles across the five study locations along the DAS cable. The top panel shows the location of the five study sites: (a) Roadside, (b) Tundra 1, (c) Tundra 2, (d) Tundra 3, and (e) Tundra 4. Middle panels show the V_s profiles estimated for geophone (solid red) and DAS (dashed blue) data. Bottom panels show the resulting seismically inferred unfrozen pore water content S_w profiles. The reference constraint is shown as a reference envelope (blue shading zone). The base map was designed and developed by Esri | Powered by Esri. For more information on this map, visit https://goto.arcgisonline.com/maps/World_Imagery (last access: 13 August 2026).

https://doi.org/10.5194/egusphere-2026-4871
Preprint. Discussion started: 14 August 2026

Table 1. Comparison metrics for paired nearby arrays: V_s root-mean-square difference (RMSD), S_w root-mean-square difference, and mean absolute S_w difference (mean $|\Delta S_w|$). The metrics were computed over a common, conservative 0-20 m depth window (considering the sensitivity depth of the inversion).

Site	RMSD V_s (m/s)	RMSD S_w	Mean $\lvert\Delta S_w\rvert$
Roadside	84.67	0.0169	0.0148
Tundra 1	125.42	0.0374	0.0326
Tundra 2	107.23	0.0243	0.0212
Tundra 3	264.49	0.0625	0.0615
Tundra 4	283.85	0.1079	0.0901

$$\Delta S_{w,\mathrm{seismic-ref}}(z) = S_{w,\mathrm{seismic,median}}(z) - S_{w,\mathrm{ref,median}}(z). \tag{5}$$

Positive values of $\Delta S_{w,\mathrm{seismic-ref}}$ indicate that the seismic-derived profile contains a larger model-inferred proportion of liquid pore water than the temperature-informed reference, whereas negative values indicate a smaller inferred unfrozen pore water fraction. We refer to these differences as reference-relative anomalies. We summarized the overall magnitude of each anomaly profile using the RMS between the temperature-informed reference model and the seismic-derived profiles. We computed the RMS only over the resolved portion of each profile (the depth interval from the surface to the 10% sensitivity kernel resolution depth listed in Table S8).

The anomaly profiles show clear site-dependent behavior along the transect (Fig. 6). Roadside, Tundra 1, and Tundra 2 show moderate departures from the reference, mostly within the shallow and intermediate subsurface. Tundra 3 shows a stronger positive anomaly in the upper part of the profile, but this anomaly decreases rapidly with depth and approaches, or locally falls below, the reference below approximately 20 m. In contrast, Tundra 4 shows the largest reference-relative anomaly for both sensing systems, and the DAS-derived anomaly remains positive through much of the interpreted model interval, consistent with the greater resolution depth of the DAS dispersion curve at this site.

The depth-dependent anomaly profiles further distinguish Tundra 4 from the other sites. At Roadside, the anomalies are positive in the upper 15 m but approach zero between approximately 15 and 22 m (Fig. 6). Tundra 1 and Tundra 2 show predominantly positive anomalies in the shallow and intermediate subsurface, followed by smaller departures at greater depths. The anomaly at Tundra 3 is mainly concentrated in the shallow-to-intermediate interval, whereas the Tundra 4 anomaly is both stronger and more persistent at depth. The full-interval and RMS values calculated over separate depth ranges are reported in Fig. 6 and Table S6, but the key result is that the site closest to the coast exhibits the strongest departure from the common reference, remaining above the reference to greater depth for both paired locations. This pattern suggests that local temperature and laboratory-derived freezing behavior alone do not fully explain the modeled ice–water partitioning at Tundra 4.

https://doi.org/10.5194/egusphere-2026-4871
Preprint. Discussion started: 14 August 2026

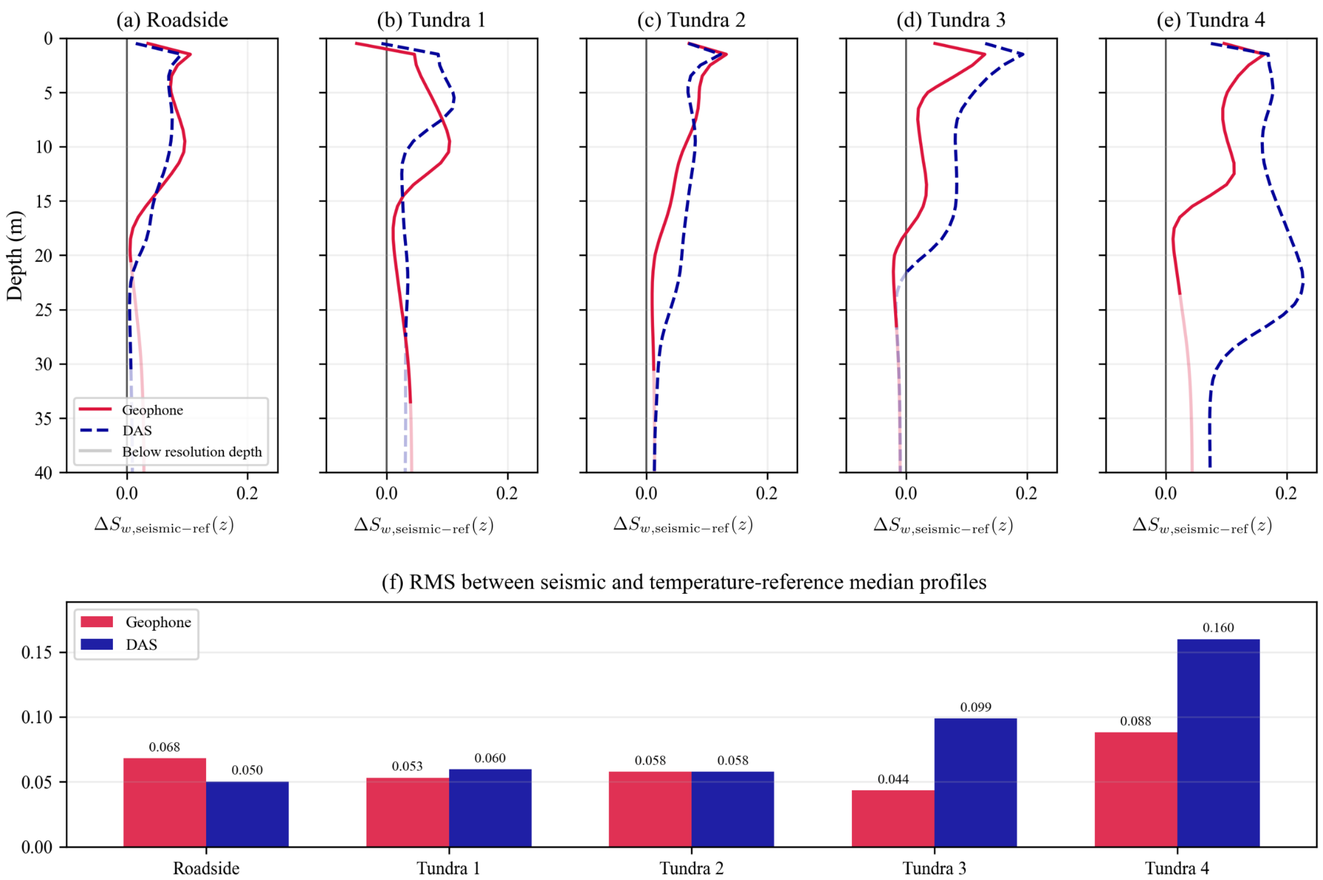

Figure 6. Reference-relative anomalies in model-inferred unfrozen pore water content at the five study locations. Panels (a)-(e) show the difference between the median seismic-derived and temperature-informed reference profiles, $\Delta S_{w,\mathrm{seismic-ref}} = S_{w,\mathrm{seismic,median}} - S_{w,\mathrm{ref,median}}$, for the geophone (solid red) and DAS (dashed blue) results. (f) RMS between the seismic and reference median profiles, computed only over the resolved portion of each profile. The DAS-derived RMS shows an overall increase toward the coastal end of the transect, whereas the geophone-derived values do not show a consistent trend of increase or decrease along the transect. Tundra 4 has the largest RMS for both sensors.

https://doi.org/10.5194/egusphere-2026-4871
Preprint. Discussion started: 14 August 2026

4 Discussion

4.1 Interpretation of the paired DAS–geophone comparisons

The paired DAS–geophone comparisons show that small-scale subsurface contrasts are spatially organized along the transect. The magnitude of paired V_s and S_w differences is not proportional to lateral offset: Tundra 1, with the largest separation (∼44 m), shows a comparatively moderate contrast, whereas Tundra 3, at only ∼15 m offset, shows a substantially larger one. This indicates that the degree of local variability reflects subsurface structure rather than acquisition geometry.

Two non-spatial factors deserve explicit consideration. First, the DAS and geophone systems differ in frequency content, spatial aperture, and near-surface coupling, which affect their effective depth sensitivity and the subsurface volume each measurement weights. These differences alone could produce systematic offsets between sensing systems, independently of any subsurface heterogeneity. Second, the surveys were acquired two years apart (August 2022 for geophones, August 2024 for DAS). In a rapidly changing Arctic coastal environment, real changes in active-layer thickness, pore water salinity, or subsurface hydrology could occur over this interval. We evaluated this using available environmental context: mean annual air temperatures at Utqiaġvik between 2022 and 2024 fell within recent decadal variability, and active-layer thickness measurements near the transect showed no statistically significant trend between the two survey years (Ji, 2025). Critically, if unfrozen water content were laterally uniform across the sites and temporal drift were driving the paired differences, a roughly uniform signal would be expected across all five sites. The lack of a transect-wide systematic offset argues against a simple uniform temporal drift, although spatially heterogeneous interannual changes cannot be excluded.

The most conservative interpretation is therefore that both sensing systems identify the coastal end of the transect, especially Tundra 4, as anomalous and depth-persistent relative to the roadside site. Whether the progression between those end members is strictly monotonic cannot be established from the geophone data alone. However, the spatial selectivity of the strongest paired contrasts supports the broader interpretation of increasing local subsurface heterogeneity toward the coast.

4.2 Depth distribution of the anomalies at Tundra 3 and Tundra 4

The depth distribution of the anomalies distinguishes Tundra 4 from the rest of the transect. At Roadside, Tundra 1, and Tundra 2, reference-relative anomalies are mostly confined to the shallow and intermediate subsurface. At Tundra 3, the positive anomaly is concentrated above approximately 20 m and approaches the reference toward the limit of the resolved depth at this site (21–26 m; Table S8). However, whether the anomaly persists beyond this depth cannot be assessed with the present data. Tundra 4 is distinct: the departure is stronger than at the other sites for both sensing systems, and the DAS-derived anomaly is sustained through much of the depth range, consistent with the greater resolution depth of the DAS dispersion curve at this site. The geophone-derived anomaly at Tundra 4 is also elevated, but the dispersion data constrain the geophone profile only to shallower depths, so we do not extend the depth-persistence claim to the geophone. This vertical distinction is central to the argument that the coastal end of the transect is not simply more anomalous near the surface, but exhibits a qualitatively different subsurface regime that is not captured by the adopted laterally uniform temperature- and laboratory-informed reference.

https://doi.org/10.5194/egusphere-2026-4871
Preprint. Discussion started: 14 August 2026

4.3 Environmental controls, limitations, and relation to prior work

The spatial organization of the anomalies is consistent with controls not fully represented by the common thermal reference. In particular, the strongest and deepest positive anomalies occur beneath the more water-rich coastal tundra, where the surface is characterized by ponds and lakes, whereas the drier roadside and inland tundra sites show comparatively smaller departures from the reference.

Salinity is a physically plausible contributor because freezing-point depression can maintain larger unfrozen water fractions at subzero temperatures, particularly in coastal sediments influenced by marine deposition, saline groundwater, or cryopeg-like conditions. The pore water salinities reported by Wang et al. (2025) confirm that saline conditions occur in the shallow local permafrost. However, the available measurements do not define a spatial salinity gradient along the transect or directly constrain conditions below 1.5 m depth. Variations in sediment texture, mineralogy, cryostructure, and ground-ice content may similarly produce site-dependent freezing behavior and elastic properties at similar temperatures. Lateral hydrologic exchange and surface-water features such as thermokarst lakes and polygonal ponds could further modify local heat and solute transport (Pedrazas et al., 2020; Siewert et al., 2021). Degradation-related changes remain a possible contributor to the positive anomalies, but separating them from saline, lithological, or hydrological controls will require direct measurements of deep salinity, repeated temperature measurements, or targeted geochemical sampling. Future work combining seismic observations with ERT and direct deep salinity/lithology measurements could help separate these controls.

Previous observations near Utqiaġvik provide useful context. Tourei et al. (2024) documented shallow spatial variability in seismic and electrical properties, while Gou et al. (2026) showed that the soil temperature field does not form a laterally uniform thermocline along the roadside. The laboratory measurements of Wang et al. (2025) further confirm that unfrozen pore water content varies among local sediment samples and is sensitive to material and hydrochemical properties. The present study extends this picture by explicitly comparing seismic-derived S_w profiles against a local thermal and laboratory reference, and by showing that the magnitude and depth extent of the departures are spatially organized rather than random.

Three limitations bound the interpretation. First, the V_s–S_w mapping is non-unique and depends on the adopted rock-physics framework, porosity regularization, and $S_{w,\mathrm{ref}}$ constraint. Because the temperature- and laboratory-informed $S_{w,\mathrm{ref}}$ reference enters the porosity objective function, the final S_w profiles are partially pulled toward the reference; the anomalies should therefore be interpreted as departures that persist after regularization. We performed a robustness check, using site-specific $S_{w,\mathrm{ref}}$ profiles built only from core samples near each site rather than a single common reference, which produced S_w profiles that remained closely similar to those from the original common reference at all sites (Figure S4), indicating that the spatial pattern reported here is not an artifact of joining samples from different locations into a single reference. Second, the reference freezing curves are derived from cores limited to the uppermost $\sim$1.5 m, and the reference relies on vertical extrapolation of shallow sediment properties across the full investigated depth. The anomaly at Tundra 4 therefore occurs precisely where the reference has no direct sediment-derived constraint, and the possibility that it partly reflects unsampled lithological change with depth cannot be excluded. Third, the depth range directly constrained by the dispersion data varies by site and sensor. Using Rayleigh-wave phase-velocity sensitivity kernels (Figure S8, Table S8), the dispersion curve retains at least 10% of its

https://doi.org/10.5194/egusphere-2026-4871
Preprint. Discussion started: 14 August 2026

peak sensitivity to 40 m only for the DAS profiles at Tundra 2 and Tundra 4; all other site-sensor combinations lose sensitivity at shallower depths (∼20-33 m). The central claim that the Tundra 4 anomaly persists through much of the deeper interpreted range is therefore best supported by the DAS profile specifically; the corresponding geophone profile, and the 20-40 m portion of the results at other sites, should be interpreted with this resolution limit in mind.

Figure 7 summarizes the key finding of this study by contrasting a laterally uniform, local SFCC-based temperature and laboratory reference with the seismic anomalies observed along the transect. Panel (a) shows the $S_{w,\mathrm{ref}}$ profile obtained by combining local borehole temperatures with laboratory freezing curves, the null hypothesis that temperature and shallow measured freezing behavior are sufficient to characterize ice–water partitioning along the transect. Panel (b) shows the seismically inferred reference-relative anomalies $\Delta S_{w,\mathrm{seismic-ref}}$, as a function of site and depth, with shading representing anomaly magnitude relative to the reference rather than absolute S_w. The figure makes the central pattern visible at a glance: the strongest small-scale subsurface heterogeneity occurs at the coastal end of the transect, and the deepest anomaly occurs at Tundra 4. The lower markers, summarizing paired DAS–geophone V_s RMSD and mean $|\Delta S_w|$, co-locate with the largest reference-relative anomalies at the same coastal sites. Although these two metrics are not fully independent, since both are derived from the same seismic profiles and rock-physics mapping, their spatial correspondence reinforces the interpretation that the coastal portion of the transect is characterized by greater local subsurface complexity at depth. The results indicate that a temperature/SFCC-based reference alone does not capture the spatial pattern of the seismic observations, particularly at Tundra 4.

5 Conclusions

We applied active-source MASW using DAS and geophone data at five sites along a roadside-to-coast tundra transect in Utqiaġvik, Alaska, and converted the resulting V_s profiles into seismically inferred unfrozen pore water content, S_w. Comparison with a common temperature- and laboratory-informed reference shows spatially organized departures from the reference, with the strongest anomaly at the site closest to the coast, Tundra 4. The DAS-derived anomaly at Tundra 4 remains above the reference through much of the deeper sensitivity-supported interval, whereas the geophone-derived result supports Tundra 4 as anomalous mainly within its shallower resolved range. The paired DAS–geophone comparisons further indicate that small-scale subsurface variability is also greatest at the coastal end of the transect. Together, these results show that a laterally uniform temperature- and shallow-laboratory reference does not fully explain the observed permafrost structure, particularly beneath water-rich coastal tundra surfaces characterized by ponds and lakes. Although salinity, sediment properties, hydrology, cryostructure, and degradation-related changes may all contribute, their relative roles remain unresolved. More broadly, the reference-anomaly framework introduced here provides a practical way to integrate seismic, thermal, and laboratory observations to characterize deep, laterally variable permafrost structure.

https://doi.org/10.5194/egusphere-2026-4871
Preprint. Discussion started: 14 August 2026

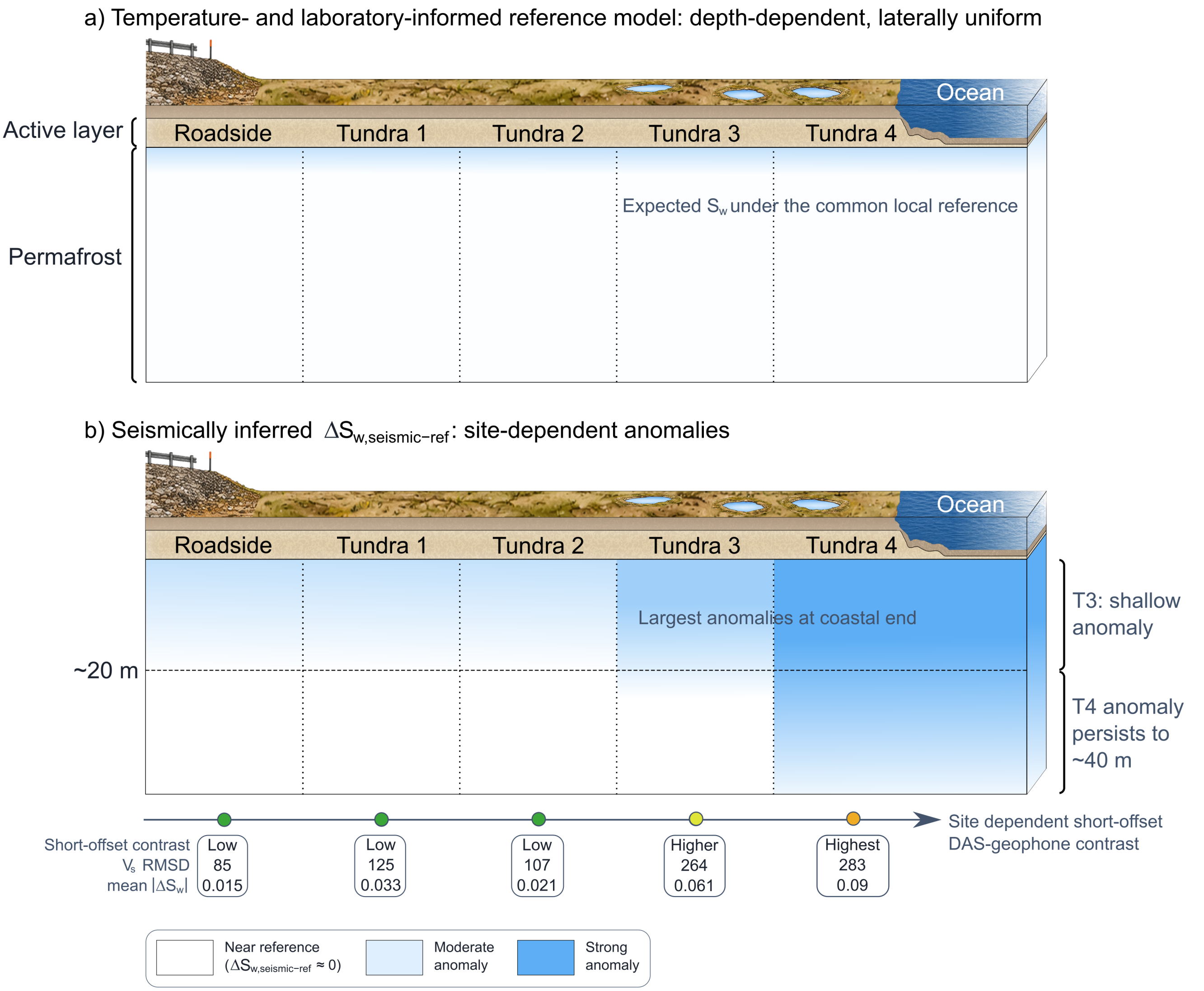

Figure 7. Conceptual summary of the S_w reference model and the reference-relative seismic anomalies along the Utqiaġvik transect. (a) The temperature- and laboratory-informed reference model represents the expected unfrozen pore water content $S_{w,\mathrm{ref}}$ as a depth-dependent but laterally uniform benchmark across the five study sites. (b) The seismically inferred reference-relative anomaly, $\Delta S_{w,\mathrm{seismic-ref}} = S_{w,\mathrm{seismic,median}} - S_{w,\mathrm{ref,median}}$, summarizes how the seismic-derived profiles depart from the common reference. Shading in panel (b) therefore represents positive anomaly magnitude relative to the reference, not absolute S_w. Roadside through Tundra 2 show comparatively small-to-moderate anomalies; Tundra 3 shows an anomaly concentrated mainly above approximately 20 m, and Tundra 4 shows the strongest anomaly, with the DAS-derived departure extending to the greatest depth. The lower markers summarize the site-dependent magnitude of the short-offset DAS–geophone contrast using the paired-profile V_s RMSD and mean $|\Delta S_w|$. The schematic summarizes patterns observed at five discrete sites and should not be interpreted as a continuous 2D inversion of S_w or ΔS_w along the full transect.

https://doi.org/10.5194/egusphere-2026-4871
Preprint. Discussion started: 14 August 2026

Code availability. The codes for reproducing the main figures and results of this study are available from https://github.com/GuilhermeZakarewicz/das-geophone-masw-permafrost.

Data availability. The processed data products and scripts used to reproduce the main results and figures are available at https://doi.org/10.5281/zenodo.21877022. The repository includes processed waveform examples, dispersion images, picked dispersion curves, inversion outputs, MASW-derived V_s profiles, temperature-derived reference constraint products, joint porosity inversion outputs, final S_w profiles, pseudo-2D Roadside products, and scripts/notebooks used to reproduce the figures. Borehole temperature data are provided by the Permafrost Laboratory, Geophysical Institute, University of Alaska Fairbanks (https://permafrost.gi.alaska.edu/).

Author contributions. G.Z.: Methodology, Software, Formal analysis, Data curation, Visualization, Writing – original draft, Writing – review and editing. G.R.S.: Software, Formal analysis, Investigation, Data curation, Writing – review and editing. M.X.: Methodology, Funding acquisition, Writing – review and editing. E.R.M.: Methodology, Funding acquisition, Writing – review and editing. T.Z.: Conceptualization, Methodology, Validation, Resources, Supervision, Funding acquisition, Writing – review and editing. All authors discussed the results, revised the manuscript, and approved the final version.

Competing interests. The authors declare no competing interests.

Acknowledgements. We thank Ahmad Tourei for providing the geophone shot-gather data used in the MASW analysis. We thank Dmitry Nicolsky for providing the borehole temperature data used to construct the temperature-depth profile. We also thank Ziyi Wang for providing the permafrost core data, including unfrozen water content measurements and the fitted power-law parameters used to construct the temperature-derived reference constraint applied in the V_s–S_w inversion. These data contributions were essential for the analyses presented in this study. This study was supported by NSF under CMMI-2034363, CMMI-2034366, and CMMI-2034380. We gratefully acknowledge the support and facilities provided by UIC Science, LLC, NOAA, and the ARM Climate Research Facility of the DOE. We thank Ahmad Tourei, Xiaohang Ji, Min Liew, Nolan Roth, Anne Jensen, Matthew Hallissey, and Chris McComb for field support.

References

AMAP: Key trends and impacts, Summary for Policy-Makers, Arctic Monitoring and Assessment Programme (AMAP), 16, 2021.

Angelopoulos, M., Overduin, P. P., Jenrich, M., Nitze, I., Günther, F., Strauss, J., Westermann, S., Schirrmeister, L., Kholodov, A., Krautblatter, M., Grigoriev, M. N., and Grosse, G.: Onshore Thermokarst Primes Subsea Permafrost Degradation, Geophysical Research Letters, 48, e2021GL093 881, https://doi.org/https://doi.org/10.1029/2021GL093881, e2021GL093881 2021GL093881, 2021.

Bartsch, A., Strozzi, T., and Nitze, I.: Permafrost monitoring from space, Surveys in Geophysics, 44, 1579–1613, 2023.

Biskaborn, B. K., Smith, S. L., Noetzli, J., Matthes, H., Vieira, G., Streletskiy, D. A., Schoeneich, P., Romanovsky, V. E., Lewkowicz, A. G., Abramov, A., et al.: Permafrost is warming at a global scale, Nature communications, 10, 264, 2019.

Brown, J., Sidlauskas, F. J., and Delinski, G.: Circum-arctic map of permafrost and ground ice conditions, US Geological Survey Reston, VA, 1997.

Carcione, J. M. and Seriani, G.: Seismic and ultrasonic velocities in permafrost, Geophysical Prospecting, 46, 441–454, 1998.

Devoie, E. G., Gruber, S., and McKenzie, J. M.: A repository of measured soil freezing characteristic curves: 1921 to 2021, Earth System Science Data, 14, 3365–3377, https://doi.org/10.5194/essd-14-3365-2022, 2022.

Dou, S., Nakagawa, S., Dreger, D., and Ajo-Franklin, J.: An effective-medium model for P-wave velocities of saturated, unconsolidated saline permafrost, Geophysics, 82, EN33–EN50, https://doi.org/10.1190/geo2016-0474.1, 2017.

Dvorkin, J. and Nur, A.: Elasticity of high-porosity sandstones; theory for two North Sea data sets, Geophysics, 61, 1363–1370, https://doi.org/10.1190/1.1444059, 1996.

Freitas, N. L., Walter Anthony, K., Lenz, J., Porras, R. C., and Torn, M. S.: Substantial and overlooked greenhouse gas emissions from deep Arctic lake sediment, Nature Geoscience, 18, 65–71, 2025.

Gou, L., Xiao, M., Zhu, T., Martin, E. R., Wang, Z., Rocha dos Santos, G., Nicolsky, D., and Ji, X.: Physics-Informed Digital Twin for Predicting Permafrost Thermodynamic Characteristics Under an Embankment Road in Utqiaġvik, Alaska, Journal of Geophysical Research: Earth Surface, 131, e2025JF008 787, https://doi.org/https://doi.org/10.1029/2025JF008787, e2025JF008787 2025JF008787, 2026.

Grosse, G., Romanovsky, V., Jorgenson, T., Anthony, K. W., Brown, J., and Overduin, P. P.: Vulnerability and feedbacks of permafrost to climate change, Eos, Transactions American Geophysical Union, 92, 73–74, 2011.

Helgerud, M. B., Dvorkin, J., Nur, A., Sakai, A., and Collett, T.: Elastic-wave velocity in marine sediments with gas hydrates: Effective medium modeling, Geophysical Research Letters, 26, 2021–2024, https://doi.org/https://doi.org/10.1029/1999GL900421, 1999.

Hugelius, G., Strauss, J., Zubrzycki, S., Harden, J. W., Schuur, E. A., Ping, C.-L., Schirrmeister, L., Grosse, G., Michaelson, G. J., Koven, C. D., et al.: Estimated stocks of circumpolar permafrost carbon with quantified uncertainty ranges and identified data gaps, Biogeosciences, 11, 6573–6593, 2014.

in 't Zandt, M. H., Liebner, S., and Welte, C. U.: Roles of Thermokarst Lakes in a Warming World, Trends in Microbiology, 28, 769–779, https://doi.org/https://doi.org/10.1016/j.tim.2020.04.002, 2020.

Jafarov, E., Parsekian, A., Schaefer, K., Liu, L., Chen, A., Panda, S., and Zhang, T.: Pre-ABoVE: Active Layer Thickness and Soil Water Content, Barrow, Alaska, 2013, ORNL DAAC, 2018.

Ji, X.: Understanding Seasonal Variations of In-Situ Thermal and Seismic Characteristics of Degrading Permafrost in the Arctic Based on Distributed Fiber Optic Sensing, Ph.D. dissertation, The Pennsylvania State University, University Park, PA, USA, https://etda.libraries.psu.edu/catalog/20330xbj5039, 2025.

https://doi.org/10.5194/egusphere-2026-4871
Preprint. Discussion started: 14 August 2026

Ji, X., Xiao, M., Martin, E. R., and Zhu, T.: Statistical evaluation of seismic velocity models of permafrost, Journal of Cold Regions Engineering, 38, 04024 021, 2024.

Jones, B. M., Kanevskiy, M. Z., Parsekian, A. D., Bergstedt, H., Ward Jones, M. K., Rangel, R. C., Hinkel, K. M., and Shur, Y.: Rapid Saline Permafrost Thaw Below a Shallow Thermokarst Lake in Arctic Alaska, Geophysical Research Letters, 50, e2023GL105 552, https://doi.org/https://doi.org/10.1029/2023GL105552, e2023GL105552 2023GL105552, 2023.

Jorgenson, M., Yoshikawa, K., Kanevskiy, M., Shur, Y., Romanovsky, V., Marchenko, S., Grosse, G., Brown, J., and Jones, B.: Permafrost characteristics of Alaska, Proceedings of the ninth international conference on permafrost, 3, 121–122, 2008.

Ke, X., Wang, W., Niu, F., Gao, Z., Huang, W., and Cao, H.: Thermokarst lakes disturb the permafrost structure and stimulate through-talik formation in the Qinghai–Tibet Plateau, China: a hydrogeophysical investigation, The Cryosphere, 19, 4989–5002, https://doi.org/10.5194/tc-19-4989-2025, 2025.

Keating, K., Binley, A., Bense, V., Van Dam, R. L., and Christiansen, H. H.: Combined Geophysical Measurements Provide Evidence for Unfrozen Water in Permafrost in the Adventdalen Valley in Svalbard, Geophysical Research Letters, 45, 7606–7614, https://doi.org/https://doi.org/10.1029/2017GL076508, 2018.

Liu, H., Maghoul, P., and Shalaby, A.: Seismic physics-based characterization of permafrost sites using surface waves, The Cryosphere, 16, 1157–1180, https://doi.org/10.5194/tc-16-1157-2022, 2022.

Ma, J., Luo, B., Guo, Z., and He, L.: Surface wave analysis using DAS and dense nodal array recordings in near-surface active surveying, Geophysical Journal International, 246, ggag151, https://doi.org/10.1093/gji/ggag151, 2026.

Mavko, G., Mukerji, T., and Dvorkin, J.: The rock physics handbook, Cambridge university press, 1998.

Minshull, T. A., Singh, S. C., and Westbrook, G.: Seismic velocity structure at a gas hydrate reflector, offshore western Colombia, from full waveform inversion, Journal of Geophysical Research: Solid Earth, 99, 4715–4734, 1994.

Nelson, F. E., Anisimov, O. A., and Shiklomanov, N. I.: Subsidence risk from thawing permafrost, Nature, 410, 889–890, 2001.

Obu, J., Westermann, S., Bartsch, A., Berdnikov, N., Christiansen, H. H., Dashtseren, A., Delaloye, R., Elberling, B., Etzelmüller, B., Kholodov, A., et al.: Northern Hemisphere permafrost map based on TTOP modelling for 2000–2016 at 1 km 2 scale, Earth-Science Reviews, 193, 299–316, 2019.

Oldenborger, G. A. and LeBlanc, A.-M.: Monitoring changes in unfrozen water content with electrical resistivity surveys in cold continuous permafrost, Geophysical Journal International, 215, 965–977, https://doi.org/10.1093/gji/ggy321, 2018.

Park, C. B., Miller, R. D., and Xia, J.: Imaging dispersion curves of surface waves on multi-channel record, in: SEG Technical Program Expanded Abstracts 1998, pp. 1377–1380, Society of Exploration Geophysicists, 1998.

Park, C. B., Miller, R. D., and Xia, J.: Multichannel analysis of surface waves, Geophysics, 64, 800–808, 1999.

Pedrazas, M. N., Cardenas, M. B., Demir, C., Watson, J. A., Connolly, C. T., and McClelland, J. W.: Absence of ice-bonded permafrost beneath an Arctic lagoon revealed by electrical geophysics, Science Advances, 6, eabb5083, 2020.

Rantanen, M., Karpechko, A. Y., Lipponen, A., Nordling, K., Hyvärinen, O., Ruosteenoja, K., Vihma, T., and Laaksonen, A.: The Arctic has warmed nearly four times faster than the globe since 1979, Communications earth & environment, 3, 168, 2022.

Rocha dos Santos, G. and Zhu, T.: Seismic Tremors From Sea-Landfast Ice Interactions Near Utqiaġvik, Alaska, Geophysical Research Letters, 52, e2025GL117 458, https://doi.org/https://doi.org/10.1029/2025GL117458, e2025GL117458 2025GL117458, 2025.

Romanovsky, V. E. and Osterkamp, T. E.: Effects of unfrozen water on heat and mass transport processes in the active layer and permafrost, Permafrost and Periglacial Processes, 11, 219–239, https://doi.org/https://doi.org/10.1002/1099-1530(200007/09)11:3<219::AID-PPP352>3.0.CO;2-7, 2000.

https://doi.org/10.5194/egusphere-2026-4871
Preprint. Discussion started: 14 August 2026

Romanovsky, V. E., Smith, S. L., and Christiansen, H. H.: Permafrost thermal state in the polar Northern Hemisphere during the international polar year 2007–2009: a synthesis, Permafrost and Periglacial processes, 21, 106–116, 2010.

Schaefer, K., Lantuit, H., Romanovsky, V. E., Schuur, E. A., and Witt, R.: The impact of the permafrost carbon feedback on global climate, Environmental Research Letters, 9, 085 003, 2014.

Schuur, E. A., Bockheim, J., Canadell, J. G., Euskirchen, E., Field, C. B., Goryachkin, S. V., Hagemann, S., Kuhry, P., Lafleur, P. M., Lee, H., et al.: Vulnerability of permafrost carbon to climate change: Implications for the global carbon cycle, BioScience, 58, 701–714, 2008.

Siewert, M. B., Lantuit, H., Richter, A., and Hugelius, G.: Permafrost Causes Unique Fine-Scale Spatial Variability Across Tundra Soils, Global Biogeochemical Cycles, 35, e2020GB006 659, https://doi.org/https://doi.org/10.1029/2020GB006659, e2020GB006659 2020GB006659, 2021.

Tourei, A., Ji, X., Rocha dos Santos, G., Czarny, R., Rybakov, S., Wang, Z., Hallissey, M., Martin, E. R., Xiao, M., Zhu, T., et al.: Mapping permafrost variability and degradation using seismic surface waves, electrical resistivity, and temperature sensing: A case study in Arctic Alaska, Journal of Geophysical Research: Earth Surface, 129, e2023JF007 352, 2024.

Vantassel, J. P., Cox, B. R., Hubbard, P. G., and Yust, M.: Extracting high-resolution, multi-mode surface wave dispersion data from distributed acoustic sensing measurements using the multichannel analysis of surface waves, Journal of Applied Geophysics, 205, 104 776, 2022.

Wang, Z., Xiao, M., Bray, M., Nicolsky, D., and Ji, X.: Creep Deformation and Long-Term Strength of Ice-Rich Permafrost in Northern Alaska, Journal of Geotechnical and Geoenvironmental Engineering, 152, 04025 161, https://doi.org/10.1061/JGGEFK.GTENG-13324, 2025.

Wathelet, M., Chatelain, J., Cornou, C., Giulio, G. D., Guillier, B., Ohrnberger, M., and Savvaidis, A.: Geopsy: A User-Friendly Open-Source Tool Set for Ambient Vibration Processing, Seismological Research Letters, 91, 1878–1889, https://doi.org/10.1785/0220190360, 2020.

Xiao, Z., Lai, Y., and Zhang, J.: A thermodynamic model for calculating the unfrozen water content of frozen soil, Cold Regions Science and Technology, 172, 103 011, https://doi.org/https://doi.org/10.1016/j.coldregions.2020.103011, 2020.

Zimmerman, R. W. and King, M. S.: The effect of the extent of freezing on seismic velocities in unconsolidated permafrost, Geophysics, 51, 1285–1290, 1986.

Zwieback, S., Liu, L., Rouyet, L., Short, N., and Strozzi, T.: Advances in InSAR Analysis of Permafrost Terrain, Permafrost and Periglacial Processes, 35, 544–556, https://doi.org/https://doi.org/10.1002/ppp.2248, 2024.